Influence of phase decomposition on mechanical properties and oxidation resistance of WCrY SMART material

Jie Chen[1], Elena Tejado[2], Andrey Litnovsky[1], Duc Nguyen-Manh[3], Eric Prestat[3], Tamsin Whitfield[3], Jose Ygnacio Pastor[2], Martin Bram[4], Jan Willem Coenen[1], Christian Linsmeier[1], Jesus Gonzalez-Julian[4, 5]

[1] *Forschungszentrum Jülich GmbH, Institute of Fusion Energy and Nuclear Waste Management, Plasma Physics (IFN-1), D-52425 Jülich, Germany*

[2] *Universidad Politécnica de Madrid, Departamento de Ciencia de Materiales-CIME, E-28040 Madrid, Spain*

[3] *United Kingdom Atomic Energy Authority, Culham Centre for Fusion Energy, Culham campus, Abingdon, Oxon OX14 3DB, UK*

[4] *Forschungszentrum Jülich GmbH, Institute of Energy Materials and Devices, Materials Synthesis and Processing (IMD-2), D-52425 Jülich, Germany*

[5] *RWTH Aachen University, Institute of Mineral Engineering, 52074 Aachen, Germany*

Abstract

Self-passivating W-11.4Cr-0.6Y (in wt.%) alloy is a plasma-facing candidate armour material in fusion power plants. In the present work, the as-sintered material, fabricated via ball milling and field-assisted sintering, was annealed at 1000 °C for varying durations to induce phase decomposition. This process leads to the transformation of the initially homogeneous microstructure into two distinct phases: the W-rich phase (αW, Cr) and the Cr-rich phase (αCr, W). Cr-rich phases preferentially form at grain boundaries, where yttrium oxides are also located, and gradually coarsen to the submicron range with increasing annealing time. The chemical compositions of both phases remain relatively stable after 75 hours of annealing. The Cr content in (αW, Cr) is 18.6 at.% at 75 h and 17.8 at.% at 100 h. Compared to the as-sintered state, the 100h-annealed material exhibits significant softening at room temperature and demonstrates increased flexural strength across all tested temperatures, but lower fracture toughness at elevated temperatures. The oxidation behavior of the 100h-annealed material under humid air at 1000 °C reveals two stages in its TGA curve: inital growth of the inner oxide layer followed by subsequent development of the protecting chromia layer. In contrast, the as-sintered material exhibits a continuous, linear mass increase throughout the oxidation process. These findings present promising prospects of the decomposed microstructure for first wall applications.

Keywords: *Self-passivating WCrY; Plasma-facing; decomposition; Softening; Thermo-mechanical properties; Oxidation;*

1. Introduction

Self-passivating Metal Alloys with Reduced Thermo-oxidation (SMART) is a promising material candidate for the first wall armour in future fusion reactors [1]. This material is primarily composed of tungsten which has advantageous properties for plasma-facing conditions, such as high melting point, low sputtering yield, low fuel retention and good thermal conductivity [2]. Moreover, the self-passivating nature of SMART material enables it to suppress the sublimation of tungsten oxides when subject to the high-temperature oxidizing environment [3]. This key feature becomes crucial in addressing potential accidental scenarios during operation of a fusion reactor, such as loss-of-coolant events and air ingress into the vacuum chamber [4, 5], and provides the passive safety of SMART first wall materials.

To date, Cr as the passivating element (10-12 wt.%), along with the so-called reactive element (typically ≤ 1wt. %) such as Y [3, 6], Zr [7, 8], Hf [9] constitute the promising chemical compositions of SMART material with proven oxidation resistance. The fabrication of those compositions by far mainly adopts the powder-metallurgical route, i.e. mechanical alloying [10] and subsequent sintering process - either hot isostatic pressing (HIP) [11, 12] or field-assisted sintering technique (FAST) [13-16]. The resulting microstructures typically manifest itself as the predominantly solid solution phase (αW, Cr) with dispersed oxide particles of the reactive element along grain boundaries (GBs). Despite the alloying of tungsten with chromium during the milling process, the (αW, Cr) phase of SMART material is oversaturated with 10-12 wt.% Cr and thus not thermodynamically stable up to ~ 1500 ℃, as indicated by the miscibility gap in the W-Cr phase diagram in **Fig. 1**. Depending on the specific composition and temperature, (αW, Cr) phase may undergo phase separation through either nucleation and growth or spinodal decomposition mechanisms, one of the differences between which lies in whether the equilibrium composition is established over time [17].

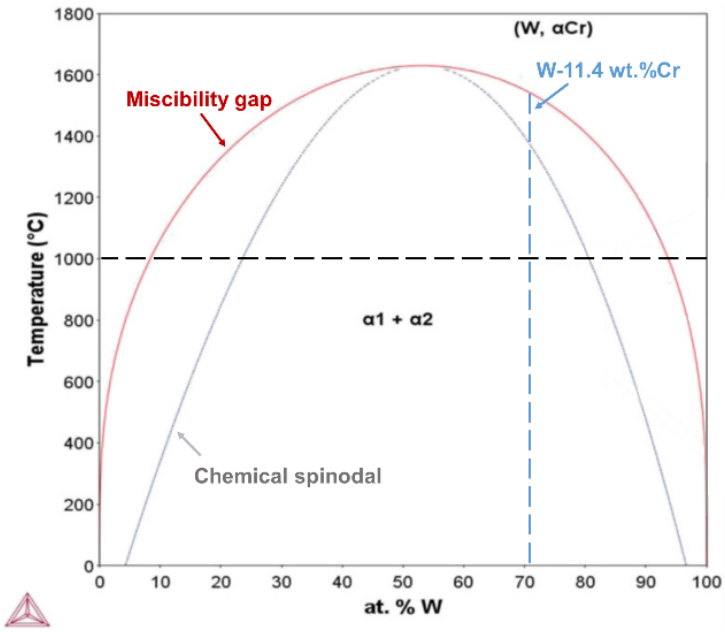

Fig. 1: W-Cr binary phase diagram [18] computed using the Thermo-Calc software [19]. The miscibility gap is marked by the red line and chemical spinodal boundary by the grey line. Yttrium solutes at 1 at.% is reported to lower the solid solution temperature of W-29Cr (at.%) by ~400 K [20]. However, as yttrium are mostly oxidized after sintering, a significant effect of yttrium on the miscibility gap could not be observed in this study.

Phase transformation of the W-Cr system with a variety of compositions has been investigated earlier [21-24]. Recent experiments, conducted by Vilémová et al. [9] and Sal et al [25], have specifically focused on the thermal stability of W-10Cr-X systems (in wt.%, with X representing reactive alloying element) for fusion relevant temperatures. Results from both studies consistently demonstrate that these compositions experience no visible microstructural change at the operational temperature of the first wall (ageing at 650 ℃ for 1000 h, 700 ℃ for 100 h) while the phase decomposition can be observed at 1000 ℃ within a relatively short time. The resultant rod-like secondary Cr-rich phase, after annealing at 1000 ℃, is reported to enhance flexural strength compared to the un-annealed single parent phase [26]. Veverka et al. further reveals that the third alloying element, despite the minor quantity, influences the decomposition rate of W-Cr solid solution [27]. For instance, alloying with Ta significantly extends the lifetime of the W-Cr solid solution during exposure at 1000 ℃ due to the mutual affinity of Cr and Ta, which acts as a diffusion barrier and hinders the growth of (αCr, W) during decomposition.

Despite the proven phase stability of SMART material during steady state operation of fusion reactors, this study explores phase decomposition in a W-11.4Cr-0.6Y alloy (in wt.%) by exposure at 1000 °C, a temperature that falls within the predicted chemical spinodal region for this composition, as illustrated in **Fig. 1**. This heat treatment temperature should exceed the operational first wall temperature under DEMO conditions, and it is only chosen to initiate phase decomposition process. This process is not expected to occur in the first wall environment and therefore needs to be intentionally induced. The microstructural and compositional evolution during different annealing stages is studied. Furthermore, we assess the thermal-mechanical properties and oxidation resistance of the decomposed material to evaluate its potential application for first wall and compare its performance to the undecomposed counterpart.

2. Experiments

For sample preparation, tungsten (99.9%, 4 μm), 11.4 wt.% chromium (99.7%, 45 μm) and 0.6 wt.% yttrium (99.9%, 500 μm) elemental powders (67.9W-31.1Cr-1.0Y in at.%) were first milled in a planetary mill (Retsch PM400 MA, Retsch GmbH, Germany) that has a rotational ratio of 1:-3. The numbers in parentheses after the elements represent the purity and particle size of the powders, respectively. The powders were enclosed in tungsten carbide coated milling jar and balls with a ball to powder ratio of 5:1. The milling process lasted for 60 h at a speed of 198 rotations per minute under Ar atmosphere. Following mechanical alloying, 25 g of the milled powders were placed into a Ø20 mm graphite mould and pressed using a hydraulic press. Then the green compact was consolidated using the filed-assisted sintering technology (FAST) (FCT-HPD5, FCT Systeme GmbH, Germany) under vacuum conditions. The powders were heated up at a ramp of 200 °C/min until reaching 1460 °C without isothermal holding at the highest temperature. The uniaxial pressure of 50 MPa was applied throughout the sintering process. The resulting ingots had a relative density over 98% measured by Archimedes' principle and retain the homogeneity achieved during the mechanical alloying process. To investigate the microstructural evolution during the decomposition process, an as-sintered ingot was sectioned into several cuboidal samples. These samples were then annealed under vacuum (10^{-6} mbar) at 1000 °C at various durations (2 h, 7 h, 14 h, 50 h, 75 h, 100 h). Annealing times of 2, 7, and 14 hours were applied to separate cuboidal samples, while the same sample was used for the 50, 75, and 100-hour annealing durations. For

bending and oxidation testing, the 100-hour annealing condition was selected and applied to the as-sintered ingots. The 100-hour annealing was conducted in multiple stages, with the total duration divided into averagely 10-hour intervals over 10 consecutive days. At the end of each day, the samples were cooled naturally along with the furnace and left inside with a vacuum maintained at 10^{-7} mbar at room temperature when not being heated.

Microstructural characterization, comprising surface and cross-sectional microstructure studies, was performed using the scanning electron microscope (SEM) equipped with a focused ion beam (FIB) (Zeiss Crossbeam XB 540, Carl Zeiss Microscopy GmbH, Germany). Some microstructural features like grain size and the size of the Cr-rich phase were further analysed using the ImageJ software [28]. X-ray diffraction (XRD) was conducted over a diffraction angle of 20° to 120° with a step size of 0.02° using D8 Discover from Bruker AXS GmbH, Germany. Elemental analyses were conducted using energy-dispersive X-ray spectroscopy (EDS) from Oxford Instruments, operated at an accelerating voltage of 12 kV. This voltage was chosen to minimize the interaction volume within the sample. Tests at a higher voltage, such as 15 kV, yielded the same chemical compositions. W M_α, Cr K_α, Y L_α and O K_α lines were selected for analysis. The "Quant Standardizations (Extended Set)" feature built in Aztec software was utilized for quantification. Note that the quantitative study of EDS has been applied only to measuring the chemical composition of (αW, Cr) throughout the presented results in this study. For (αCr, W) and yttrium oxide, due to their fine size and the use of an accelerating voltage of 12 kV, EDS analysis is not accurate quantitatively and is used only for qualitative purposes. Vegard's law [23] is used as an auxiliary method for estimation of chemical composition of (αCr, W). The data below compare the results of Vegard's law with those from EDS: The Cr content in (αW, Cr) of the as-sintered material is 23.5 at.% as deduced by Vegard's law and 29.7 at.% on average as measured by EDS, with the latter approaching the nominal value. The Cr content in (αCr, W) of the 100h-annealed material is 91.5 at.% as deduced by Vegard's law and 59.4 at.% on average as measured by EDS, with the former providing higher accuracy.

Vickers hardness of samples were determined using DuraScan G5 (ZwickRoell GmbH & Co. KG, Germany). Ten indentations were made on each sample with an applied load of 0.5 kgf (HV 0.5) for a dwell time of 10 s and the average hardness value (kgf/mm^2) was taken.

Non-standard three-point bending (TPB) tests were conducted to evaluate the flexural strength of both as-sintered and 100h-annealed materials. Miniature beams with dimensions of approximately 20 × 2.1 × 1.4 mm were cut from sintered ingots using electrical discharge machining (EDM) and later polished. These specimens were placed with a support span length of 12 mm and tested using an Instron 8862 universal testing machine (Instron, the United Kingdom) in displacement-controlled mode. Bending was performed at a strain rate of 100 μm/min under vacuum (10^{-6} mbar). The operational temperature ranged from room temperature to 1100 ℃. Flexural stress σ and linear strain ε were computed using Eq. 1

$$\sigma = \frac{3FL_s}{2BW^2} \tag{1}$$

and Eq. 2,

$$\varepsilon = \frac{6\delta W}{{L_s}^2} \tag{2}$$

respectively. Here, F is the applied force, L_s is the support span, which is 12 mm, B and W are the specimen width and thickness, respectively and δ the deflection of the bending beam. The proof flexural strength refers to the maximum stress upon brittle fracture or the yield stress when plastic deformation occurs. The yield strength is determined using the 0.2% strain offset method. In this method, a line parallel to the initial elastic region of the stress-strain curve is drawn with an offset of 0.2% strain. The intersection of this line with the curve is the 0.2% offset yield strength.

Fracture toughness measurements were performed under identical experimental conditions except that single edge laser-notched beams were used for testing instead. The notch length ranged within 150 - 400 μm and the radius of the notch tip ranged within 5-20 nm, depending on the specimen. The critical stress intensity factor K_{IQ} was calculated using the Eq. 3, as proposed by Pastor and Guinea et al. [29, 30]. Note that the critical load F_Q was captured using the 5% secant method, i.e. a 5% secant line with a slope equal to 95% of the initial elastic loading slope, when curves were non-linear.

$$K_{IQ} = \frac{3F_Q L_s \sqrt{a}}{2W^2} \frac{A - \frac{a}{W}B + \left(\frac{a}{W}\right)^2 C - \left(\frac{a}{W}\right)^3 D + \left(\frac{a}{W}\right)^4 E}{\left(1 - \frac{a}{W}\right)^{\frac{3}{2}}\left(1 + \frac{2a}{W}\right)} \tag{3}$$

Where a is the initial notch length, and:

$$A = 1.989 - 0.356\frac{W}{L_s} \quad (4)$$

$$B = 1.217 - 0.315\frac{W}{L_s} \quad (5)$$

$$C = 3.212 - 0.705\frac{W}{L_s} \quad (6)$$

$$D = 3.222 - 0.020\frac{W}{L_s} \quad (7)$$

$$E = 1.226 - 0.015\frac{W}{L_s} \quad (8)$$

The oxidation behaviour was studied using a thermogravimetric analyzer (TGA) (TAG-16, Setaram Inc., France). Cuboidal specimens with dimensions of 4.9 × 3.0 × 3.6 mm were machined from as-sintered and 100h-annealed ingots and ground to a 1200 grit surface finish [3]. Specimens were exposed to an isothermal temperature of 1000 ℃ in the synthetic air with 70% relative humidity at 25 ℃. These experimental conditions were designed to simulate accidental scenarios for the first wall. The measurement yields the *in-situ* mass change of samples – the sum of mass gain due to oxidation and the mass loss due to sublimation, as a function of time.

3. Results and discussion

3.1. Microstructures

As presented in **Fig. 2a**, the as-sintered material is characterized by an overall homogeneous (αW, Cr)$_0$ (parent phase) with average grain size of 183 nm. Yttrium undergoes oxidation during the fabrication process, and its oxides are distributed along grain boundaries (GBs). Following a 2-hour annealing treatment at 1000℃, the number density of nanosized particles within the microstructure, as shown in **Fig. 2b**, increases compared to that shown in **Fig. 2a**, due to the formation of (αCr, W). **Fig. 2b-g** illustrate progressive coarsening of (αCr, W) over extended annealing times. Statistically, (αCr, W) steadily grows from (70 ± 18) nm at 2 h to (129 ± 69) nm at 100 h. Coarsening of some (αCr, W) phases leads to a slight decrease in number and a broader

size distribution of (αCr, W). These (αCr, W) clusters, together with the existing yttrium oxides at GBs, may act to impede the growth of $(\alpha W, Cr)_0$ grains by grain boundary pinning or solute dragging mechanisms [31, 32], as original $(\alpha W, Cr)_0$ grains do not experience noticeable growth during the annealing time. The average grain size of (αW, Cr) in the material annealed for 100 hours is estimated to be 189 nm. Nevertheless, the finer (αCr, W) phases contributes to the overall refinement of the microstructure. Notably, despite weak contrast with yttrium oxides in SEM images, (αCr, W) can be distinguished by its irregular shape (vermicular in **Fig. 2b-e** and granular in **Fig. 2f-g**) and larger size. In contrast, yttrium oxides maintain a circular shape and exhibit no noticeable growth, mostly remaining smaller than 50 nm, as shown **Fig. 3b**.

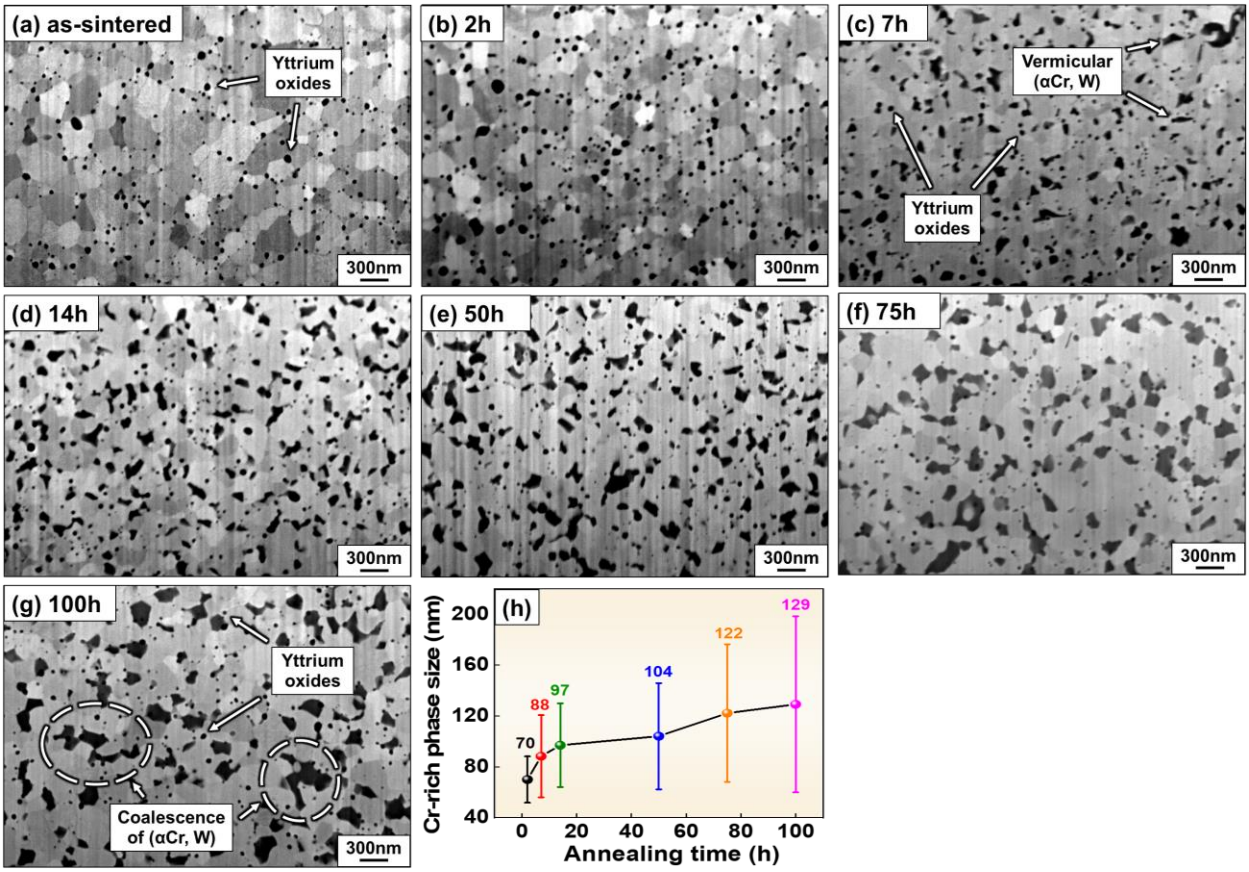

Fig. 2: Microstructures of (a) as-sintered samples and annealed samples at 1000 ℃ for (b) 2 h, (c) 7 h, (d) 14 h, (e) 50 h, (f) 75 h, (g) 100 h. (h) the evolution of average Cr-rich phase size over different annealing stages. The characteristic size of irregular (αCr, W) is defined as the diameter of a circle with surface area equal to that of the (αCr, W) phase.

Most decomposed (αCr, W) phases conspicuously appear at GBs and encircle yttrium oxides, as shown in **Fig. 3a-b**. This suggests that these interfaces, where atom diffusivity is presumably higher than in the grain interior, are preferential sites for the onset of phase decomposition. Despite the composition and temperature studied lying within the spinodal region of the phase diagram, the formation of solute clusters at GBs after annealing resembles a nucleation mechanism, as GBs provide a lower energy barrier to nucleation. On the other hand, the existing studies using phase field models have also elucidated the role of grain boundaries in initiating spinodal decomposition [33, 34]. The impact of grain boundary directed spinodal decomposition on phase transitions has been investigated [35, 36]. Therefore, further experimental study is needed to determine whether phase decomposition in the SMART material occurs via the nucleation and growth mechanism or the spinodal mechanism under the effect of grain boundary.

In addition to the GBs as the preferred decomposition site, the morphology resulting from spinodal decomposition can be grain size dependent. Studies [37, 38] have shown that the solute-rich discontinuities can form at GBs during spinodal decomposition of nanocrystalline alloys, differing from the classic lamellar patterns. Given the high population of grain boundaries in our material before decomposition and the formation of Cr-rich clusters at GBs post-decomposition, the mechanism described in Ref. [37] may apply to the decomposition process in our material if spinodal decomposition is indeed occurring. The decomposed morphology (Cr-rich discontinuities at GBs) observed in this work aligns with another investigation of a submicron-grained WCrY alloy (< 1 μm) heat-treated under the same conditions (1000℃ for 100 h) [25]. However, a study on a micron-grained W-Cr alloy (~6 μm) shows that alternating Cr-rich and Cr-lean lamellae initially forms at and perpendicular to GBs and gradually extend into the grain interior over decomposition time [27]. This highlights the grain size dependence of decomposed morphology. Interestingly, the Cr-rich phase (in small amounts and homogeneous) in the as-sintered material also undergoes spinodal decomposition. The decomposition is confined within its own region, as shown in **Fig. 3c**., resulting in a lamellar pattern characteristic of spinodal decomposition throughout the entire phase.

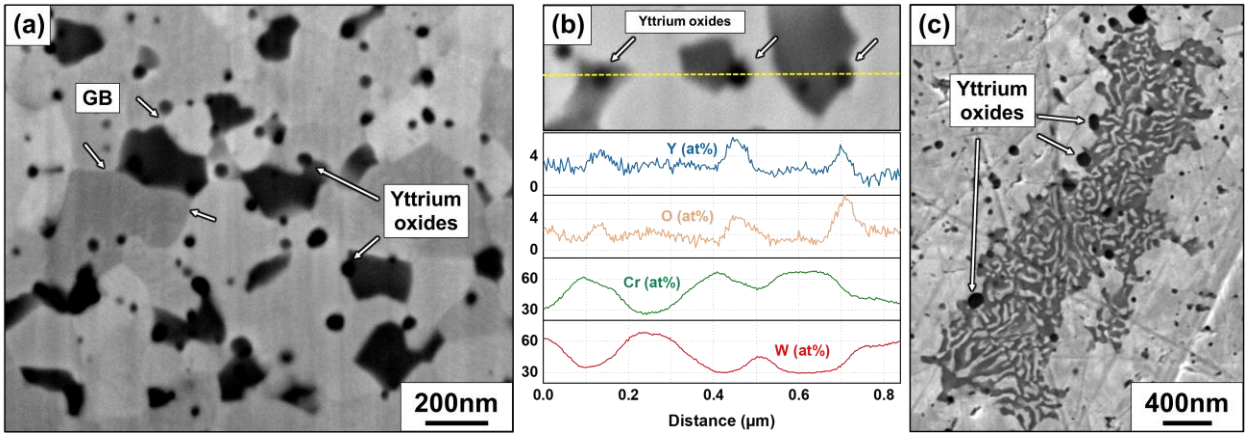

Fig. 3: The decomposed Cr-rich phase in 100h-annealed material at (a) grain boundaries and (b) yttrium oxides. As indicated by the EDS line scan in (b), the darkest circular particles correspond to the signals of Y and O. The surrounding dark phases are identified as Cr-rich clusters, while the light phase in the background is the W-rich phase. The EDS analysis here is used only for qualitative purposes. (c) spinodal decomposition within the Cr-rich phase after 2 h annealing; Note that this Cr-rich phase of ~ μm size has been pre-existing homogeneously in as-sintered material.

The evolution of lattice parameters and chemical compositions over annealing time is illustrated by means of XRD and EDS in **Fig. 4**. In **Fig. 4a**, the diffraction peak of (110) plane of $(\alpha W, Cr)_0$ in the as-sintered material is situated at 41.15°, deviating from pure W (40.3°) due to the alloying with ~30 at.% Cr. Throughout annealing, the peak shifts towards smaller angles due to the depletion of Cr until 75 h, after which no change in the peak position and lattice parameter is observed. The Cr content of (αW, Cr) decreases to (17.8 ± 1.6) at.% (measured by EDS) at 100 h, as shown in **Fig. 4c**. The equilibrium composition for (αW, Cr) is ~6.5 at.% Cr at 1000°C as per **Fig. 1**, indicating the (αW, Cr) composition is still non-equilibrium after 100 hours annealing.

Meanwhile, the decreasing Cr in (αW, Cr) forms secondary (αCr, W) phases. Initially absent in the as-sintered state by XRD (though some (αCr, W) can be still occasionally be observed in the microstructure), the (110) peak of (αCr, W) with weak intensity appears after 2 h annealing, marking the onset of phase decomposition. This is consistent with microstructural observations in **Fig. 2b**. The continuous decreasing lattice parameter seemingly supports uphill diffusion which is characteristic of spinodal decomposition mechanism, while the secondary phase is expected to establish an equilibrium composition once formed during a nucleation-driven process [17]. However, due to the very small compositional variation in (αCr, W), evidenced by limited peak

shifts in XRD spectra, this evidence for spinodal decomposition is not strong. Similar to (αW, Cr), the lattice parameter of (αCr, W) remains nearly constant after 75 h. The composition of (αCr, W) is deduced using Vegard's law [23], which is 91.5 at.% Cr, nearly reaching equilibrium at 1000°C (~92 at.% Cr). Likewise, Ref. [25] also reports non-equilibrium conditions for (αW, Cr) phases and near-equilibrium for (αCr, W) phases of W-10Cr-0.5Y under the same conditions (1000°C for 1000 hours). Despite this, the compositional stability of both phases after 75 h annealing, together with limited growth of (αCr, W) in size (**Fig. 2h**), suggests a slowdown in decomposition kinetics after 75 h.

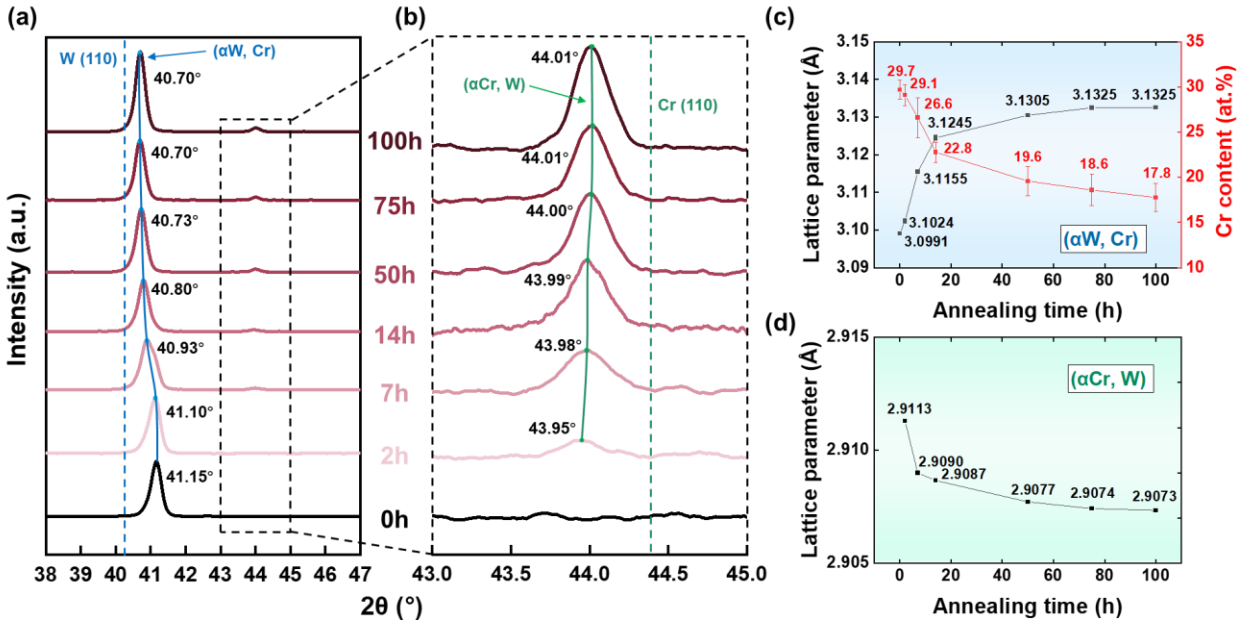

Fig. 4: (110) peak positions in XRD spectra of (a) (αW, Cr) and (b) (αCr, W) at different annealing times. Both phases have a BCC structure. Lattice parameters and Cr contents of (c) (αW, Cr) phases and (d) lattice parameters of (αCr, W) phases at different annealing stages. Lattice parameters of (αW, Cr) were calculated based on (110), (200), (211) peaks while those of (αCr, W) were calculate only using (110) peaks, the only visible peaks with weak intensity in XRD spectra. The Cr content of (αW, Cr) in (c) is measured by EDS.

3.2. Hardness

Fig. 5 shows that hardness exhibits a slight increase during the initial decomposition stages at 2 h and 7 h. This could be attributed to the dispersion hardening caused by emerging nanosized (αCr, W) particles distributed along grain boundaries of (αW, Cr). However, this effect diminishes with further coarsening of (αCr, W) and softening takes place instead. A substantial decline in hardness

is evident after 14 hours and continues up to 100 hours. This softening phenomenon, due to the coarsening decomposed phases, aligns with studies in other alloys [39]. Additionally, the compositional changes should also come into play. The initial high hardness of as-sintered material is partly due to alloying with ~30 at.% Cr. During decomposition, the depletion of Cr in (αW, Cr) reduces the solid solution hardening effect, resulting in a softer phase. This could also be indicated by the decrease in FWHM of the (110) peaks of (αW, Cr) from 0.372° in the as-sintered state to 0.340° after 100 hours of decomposition in **Fig. 4a**. This decrease suggests a release of lattice strain following the compositional change [40]. When the lattice strain is reduced, the strain-induced variation in the interplanar spacings within the (αW, Cr) lattice also decrease. This leads to less variation in the angles at which X-ray are diffracted, resulting in a narrower FWHM. In short, the coarsening of secondary (αCr, W) phases and the depletion of Cr in (αW, Cr) at the high extent of decomposition contribute to the material softening.

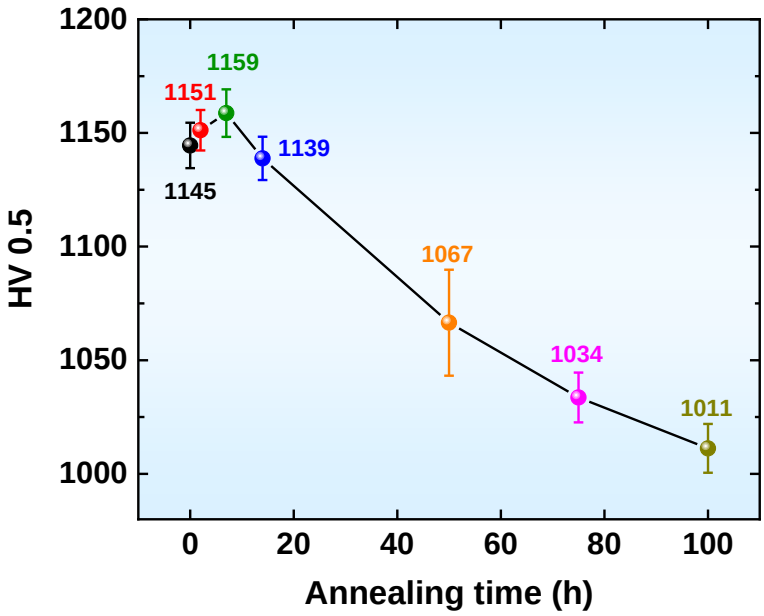

Fig. 5: The evolution of Vickers hardness (HV 0.5) over different decomposition stages.

3.3. Three point bending tests

The flexural stress – strain curves in **Fig. 6** show brittle fracture behavior for both materials up to ~900°C and clear ductility emerges at 1000 °C. This suggests that the ductile-to-brittle transition temperature (DBTT) lies between 900 °C and 1000 °C. Although the decomposed microstructure exhibits lower hardness than the undecomposed material at room temperature, there is a limited

enhancement in ductility. This may be attributed to the inherent brittleness of the (αW, Cr) and (αCr, W) phases, both having a body-centred cubic structure. Nevertheless, the flexural strength of decomposed materials, as shown in **Fig. 7a**, reaches approximately 1.1 GPa below DBTT, significantly higher than the as-sintered material's strength of 700 - 800 MPa. Above DBTT, both materials experience a notable decrease in flexural strength, with the decomposed material maintaining a slightly higher strength. The increased strength after decomposition is believed to result from refined microstructures. Even with coarsening at 100 h, the size of (αCr, W) phase remains smaller than the grain size of the parent $(\alpha W, Cr)_0$ phase, increasing the density of interfacial defects, i.e. phase boundaries, in the microstructure. Moreover, the lattice mismatch in the phase boundary between (αCr, W) and (αW, Cr), as indicated by the difference in the lattice parameters of two phases in **Fig. 4c-d**, suggests a likely incoherent interface, which impedes dislocation movement and contributes to the strengthening mechanism. Notably, the decomposed WCrY begins to exhibit higher strength from 600 ℃ than commercial Plansee W manufactured by HIP and rolling, tested in L-T direction (E. Tejado) [41]. Even in semi-decomposed stages, the material could show potential for strength improvement, with flexural strength increased by 45 - 65% for material decomposed at 1000℃ for only 15 hours (J. Veverka, et al.) [26]. It is also worth mentioning that the increase in strength is accompanied with a decrease in hardness in the decomposed SMART material, which aligns with the results in Ref. [26]. Both the solid solution and interfaces (GBs, phase boundaries) play a role in the mechanical response of the SMART material. However, the differing variations in hardness and strength after annealing suggest that for SMART materials in the decomposed state, the hardness is more susceptible to chemical composition, while the strength is more affected by the interface density. Moreover, the relative density of SMART material increases from 99.00% in the as-sintered state to 99.59% after 100 hours' annealing, which may also contribute the observed higher flexural strength.

Regarding fracture toughness, both materials exhibit values of ~5 MPa·√m at room temperature. However, at elevated temperature, the fracture toughness of the decomposed materials is about 1 MPa·√m lower than that of the as-sintered materials. As shown in **Fig. 7c**, the as-sintered material predominantly shows inter-granular crack propagation, indicating weak grain boundary cohesion in the $(\alpha W, Cr)_0$ phase. The lower fracture toughness of the decomposed material suggests that the preferential presence of (αCr, W) at grain boundaries does not provide higher crack resistance than the original grain boundaries. The (αCr, W) phases display brittle fracture behaviour even at

elevated temperatures. An example is given in **Fig. 7d,** where cleavage of (αCr, W) fractured at 400 ℃ is shown. Despite the low fracture toughness values of both materials, the difference between them remains insignificant.

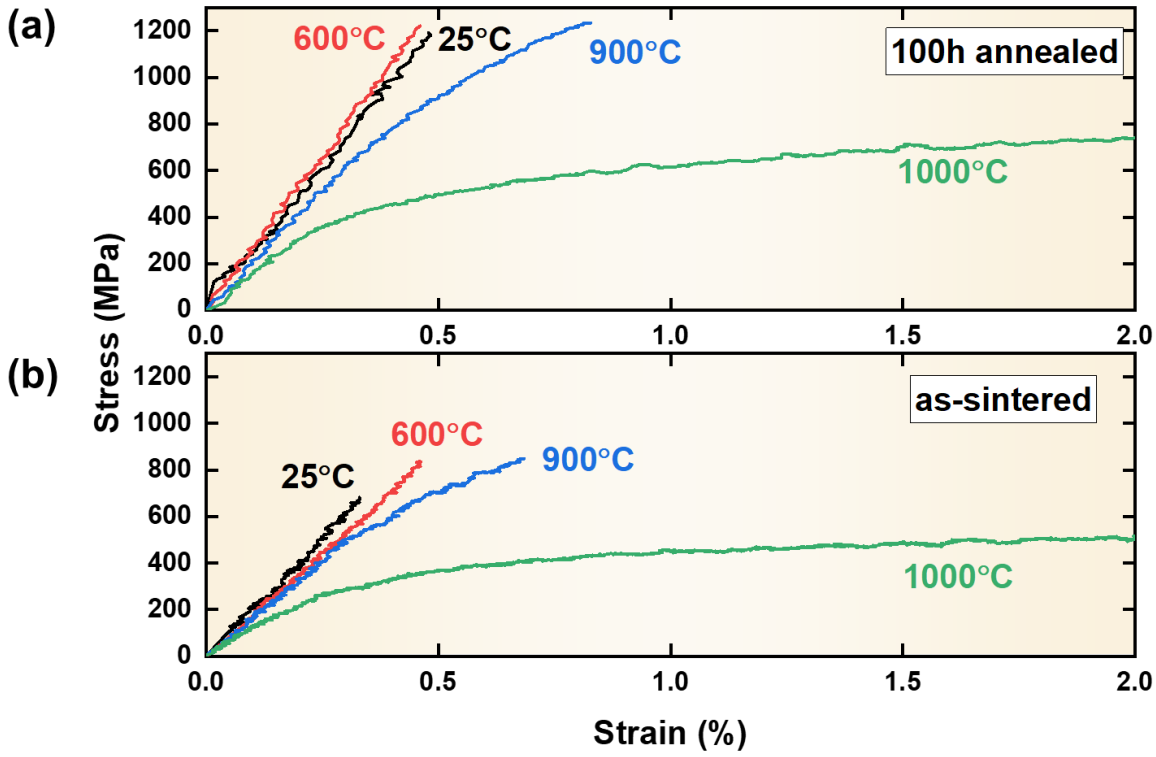

Fig. 6: Flexural stress vs. strain of (a) as-sintered and (b) 100h-annealed materials tested at 25 ℃, 600 ℃, 900 ℃ and 1000 ℃.

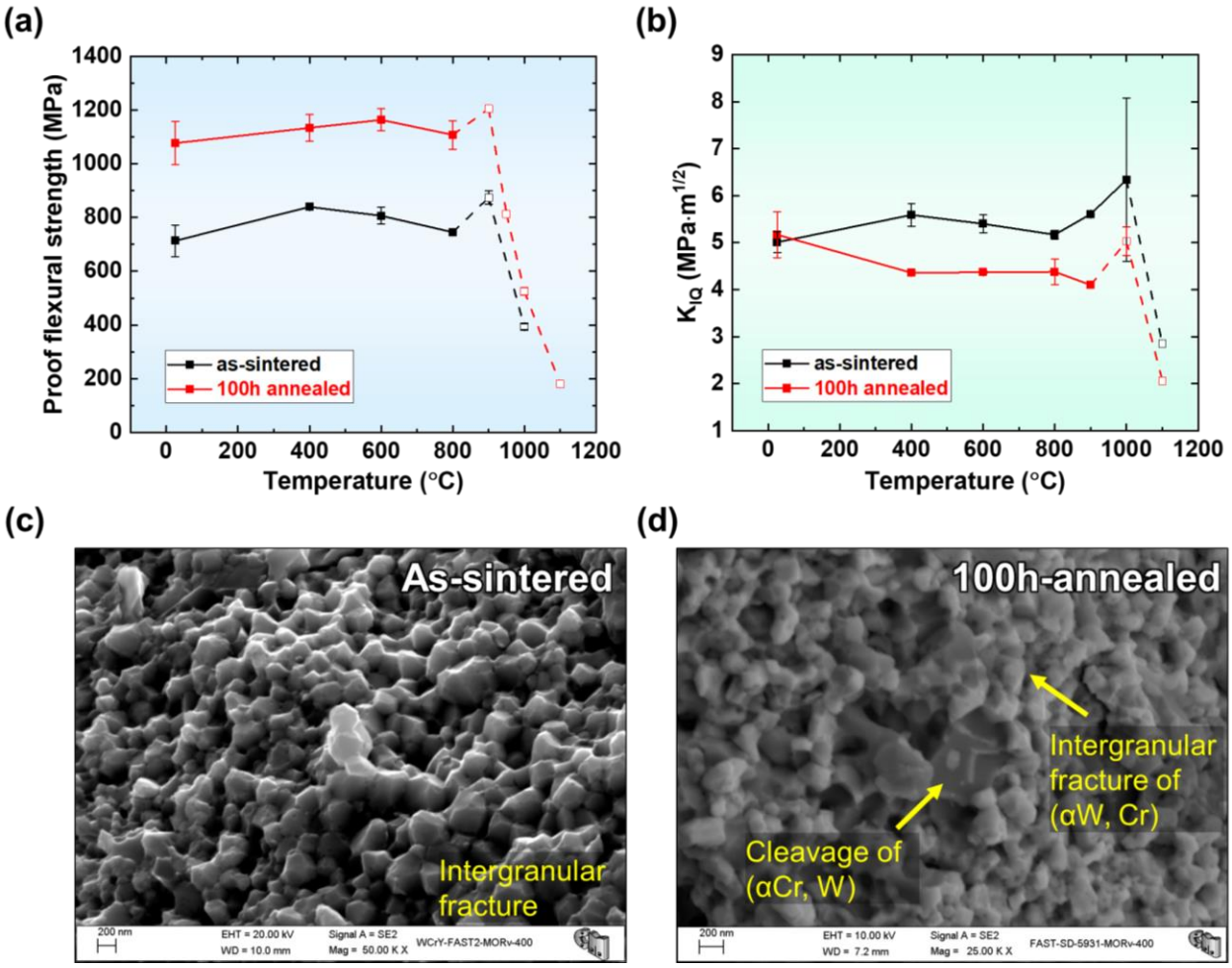

Fig. 7: (a) Flexural strength and (b) fracture toughness of as-sintered and 100h-annealed materials measured from room temperature up to 1100 °C. The figures present average values and standard error from at least two measurements. Open symbols and dashed lines indicate yield flexural strength and apparent values of fracture toughness, when non-linear behavior was observed. SEM observations of brittle fractured surfaces of (c) as-sintered and (d) 100h-annealed materials, both fractured at 400 °C.

3.4. Oxidation tests

The oxidation behaviour of the as-sintered material (**Fig. 8a**) commences with a transient oxidation stage, during which a chromium oxide scale forms on the surface within approximately 10 minutes. Following the formation of chromia scale, an overall linear oxidation pattern until 20 h is observed, interspersed with breakaway events. This initial transient oxidation phase and the subsequent linear oxidation align with the mass change pattern reported in Ref [7, 8, 42]. The linear mass increase is calculated to be 1.1×10^{-5} mg·cm^{-2}·s^{-1} over the 20-hour oxidation period. This process is

predominantly governed by the growth of the inner oxide layer, which consists of a mixed species: W-Cr-O (likely Cr_2WO_6 [6]) in the upper area and W oxides in the lower area. For the cross section shown in **Fig. 8b**, the thickness is (4.49 ± 0.86) μm for the inner oxide layer and (482 ± 232) nm for the top chromia scale after 20 hours of oxidation. These values represent the averages and the standard deviations. The TGA curve for 100h-annealed material, also shown in **Fig. 8a** for comparison, exhibits a similar main gain after 20 h, but the intermediate oxidation kinetics is different.

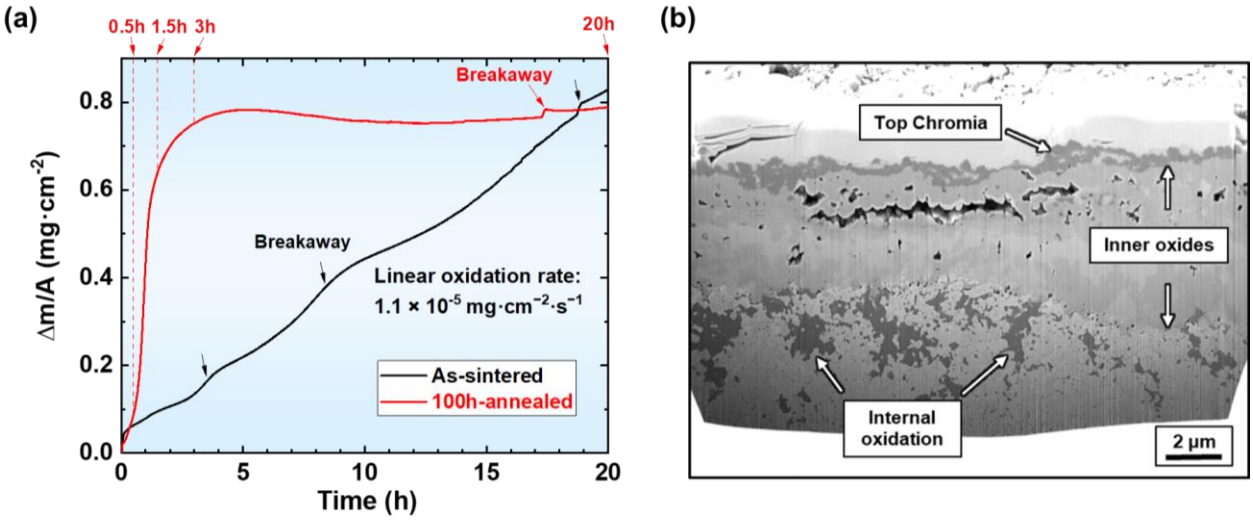

Fig. 8: (a) Specific mass change of the as-sintered and 100h-annealed material during 20 hours' oxidation, which shows different kinetics in the process but lands at the close values (~0.8 mg·cm^{-2}) at 20 h. (b) cross sectional microstructure of the as-sintered material after 20 hours oxidation.

The oxidation behavior of the decomposed material can be generally divided into two stages during the 20-hour oxidation period. The first stage (0 to 3 h) is characterized by predominant growth of inner oxides. A thin top chromia layer and an inner oxide layer are formed in 0.5 h. Between 0.5 h and 1.5 h, the inner oxide layer grows by ~ 6 μm, outpacing the slower growth of the top chromia layer (~ 85 nm), as shown in **Fig. 9**. This period yields a linear mass gain of ~ 3.0 × 10^{-4} mg·cm^{-2}·s^{-1}, which is one order of magnitude higher compared to the as-sintered material. This increased oxidation rate is due to that (αW, Cr) phase has a depleted amount of Cr after decomposition, hence reduced passivating effect and increased vulnerability to oxidation. The reduced chromium content in the WCr alloy can lead to a greater mass gain during oxidation [43]. Some decomposed (αCr, W) phases are still visible in the inner oxide layer at 1.5 h, seen in **Fig.**

10b. Notably, voids are primarily found in or near (αCr, W) phases in the inner oxide layer, as shown in cross sectional view at 1.5 h in **Fig. 10a**. They resemble Kirkendall voids, formed as Cr atoms diffuse away from (αCr, W) phases towards the surface while the influx of W atoms to (αCr, W) phases is low.

After 1.5 h, the linear mass gain gradually transitions to a significantly reduced oxidation rate. The transition can be understood by comparing the cross sectional microstructures at 1.5 h and 3h. Proceeding to 3 h, (αCr, W) are almost entirely absent and a pronounced Cr concentration gradient (high to low) is established in the inner oxide layer from top to bottom, as evidenced in **Fig. 10c**. This signifies the complete dissolution of (αCr, W) phases and subsequent upward diffusion of Cr atoms after 1.5 h. It is possible that the inward-diffusing oxygen then reacts with this Cr-rich region to form oxides, reducing the likelihood of further inward diffusion to oxidize the (αW, Cr) in the substrate alloy. Consequently, the linear oxidation observed from 0.5 to 1.5 h slows down after 1.5 h. This deceleration in kinetics, attributed to the upward diffusion of Cr from the decomposed (αCr, W) phases, is not seen in the oxidation of as-sintered homogeneous microstructure which shows a continuous linear mass increase throughout the 20-hour period. Additionally, at 1.5 h, Y signals are not detected in the Cr-rich region but are associated with W oxides in the lower part of the inner oxide layer in weak intensity, as shown in **Fig. 10c**. This may suggest that Y primarily forms W-Y-O compounds in the inner oxide layer during oxidation of the decomposed material.

The second stage (3 to 20 h) is characterized by the ongoing expansion of the top chromia scale and the decreased thickness of the inner oxide layer. The chromia scale thickness increases to (1338 ± 460) nm at 20 h, ~3 times thicker compared to the oxidized as-sintered material at the same oxidation time. The buckling morphology, observed on the oxidized surface at 20 h in **Fig. 11**, is likely a result of the compressive growth stress developing within the chromia scale [44]. The reduction in thickness of the inner oxide layer predominantly occurs in the Cr-rich region, which decreases from ~ 4 μm at 3 h to less than 2 μm at 20 h. This, along with the thickening of the top chromia layer, may suggest that the Cr-rich region in the inner oxide layer has been oxidized during this stage and gradually "transformed" into the chromia scale on the top. The growth process of the chromia scale appears sluggish, with a specific mass grain of only 0.036 $mg \cdot cm^{-2}$ attained between 3 h and 20 h. The TGA curve between 5 h to 10 h even indicates a decline rate of 1.4×10^{-6} $mg \cdot cm^{-2} \cdot s^{-1}$, closely aligning with the Cr_2O_3 volatilization rate of $2 \times 10^{-}$

^{6} mg·cm^{-2}·s^{-1} and two orders of magnitude lower than WO_3 sublimation rate [45]. After 10 h, some breakaway and self-healing events occur and cause abrupt but intermittent increase in mass, shown in **Fig. 8a**. Signs of the breakaway event include some collapse bumps found on the oxidized surface at 20 h in **Fig. 11**, possibly resulting from extensive scale buckling or spallation.

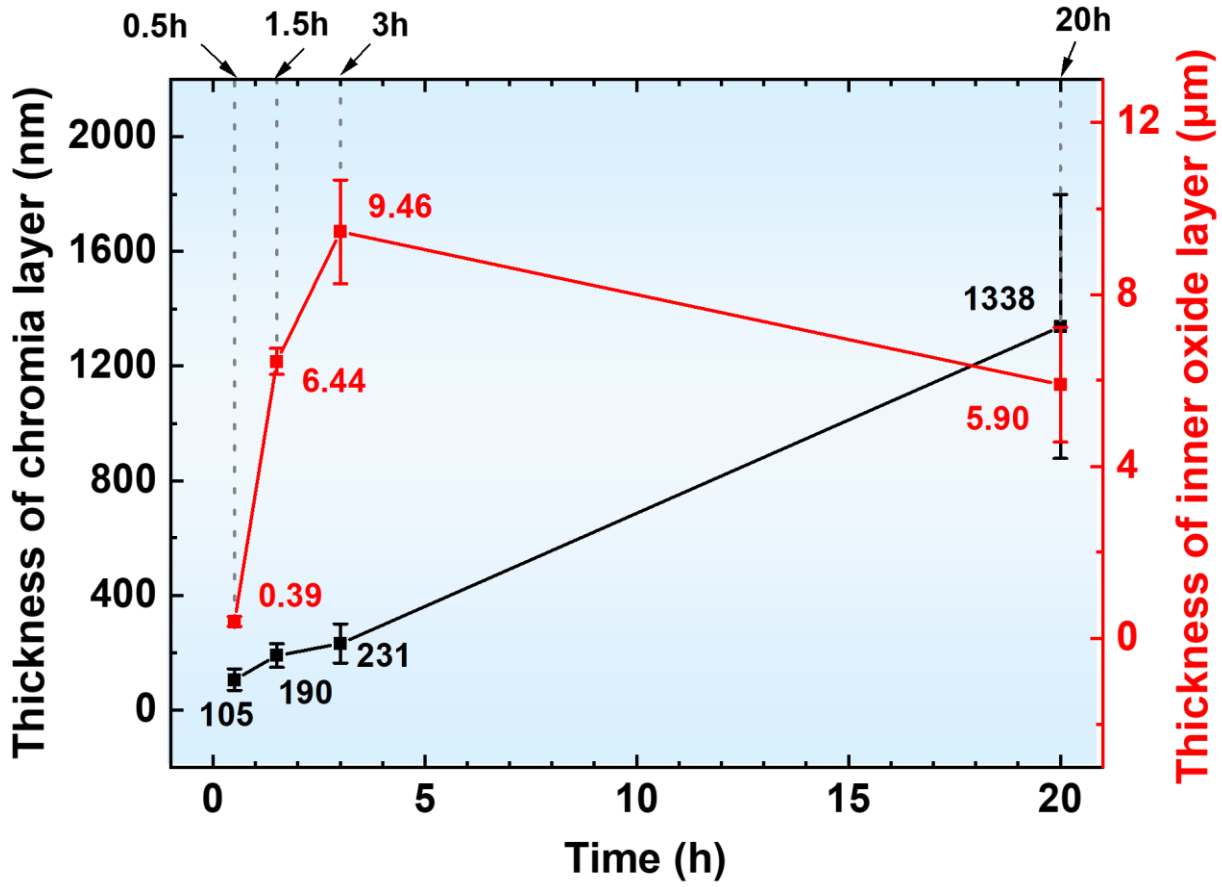

390

Fig. 9: The thickness of the top chromia and inner oxide layer at different oxidation stages of the 100h-annealed material. The figures present average values and standard deviations from ten measurements.

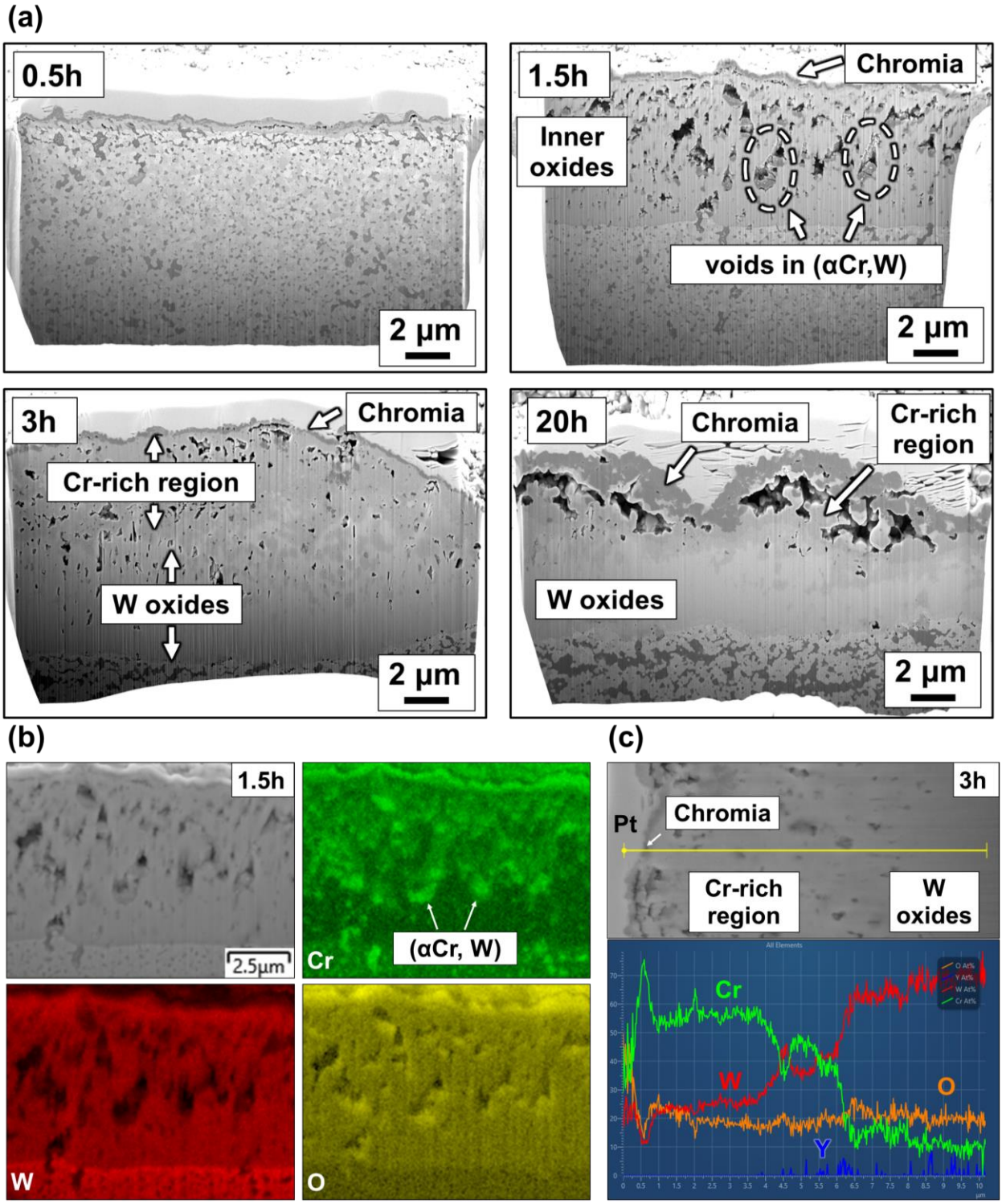

Fig. 10: (a) Cross section views of microstructural evolution at different oxidation stages of the 100h-annealed material. (b) EDS mapping of the cross section at 1.5 h. (αCr, W) is present in the inner oxide layer. (c) EDS line scan of the cross section at 3 h, from top (left) to bottom (right). The variation in elemental concentrations shows a Cr-rich region in the upper area of the inner oxide layer.

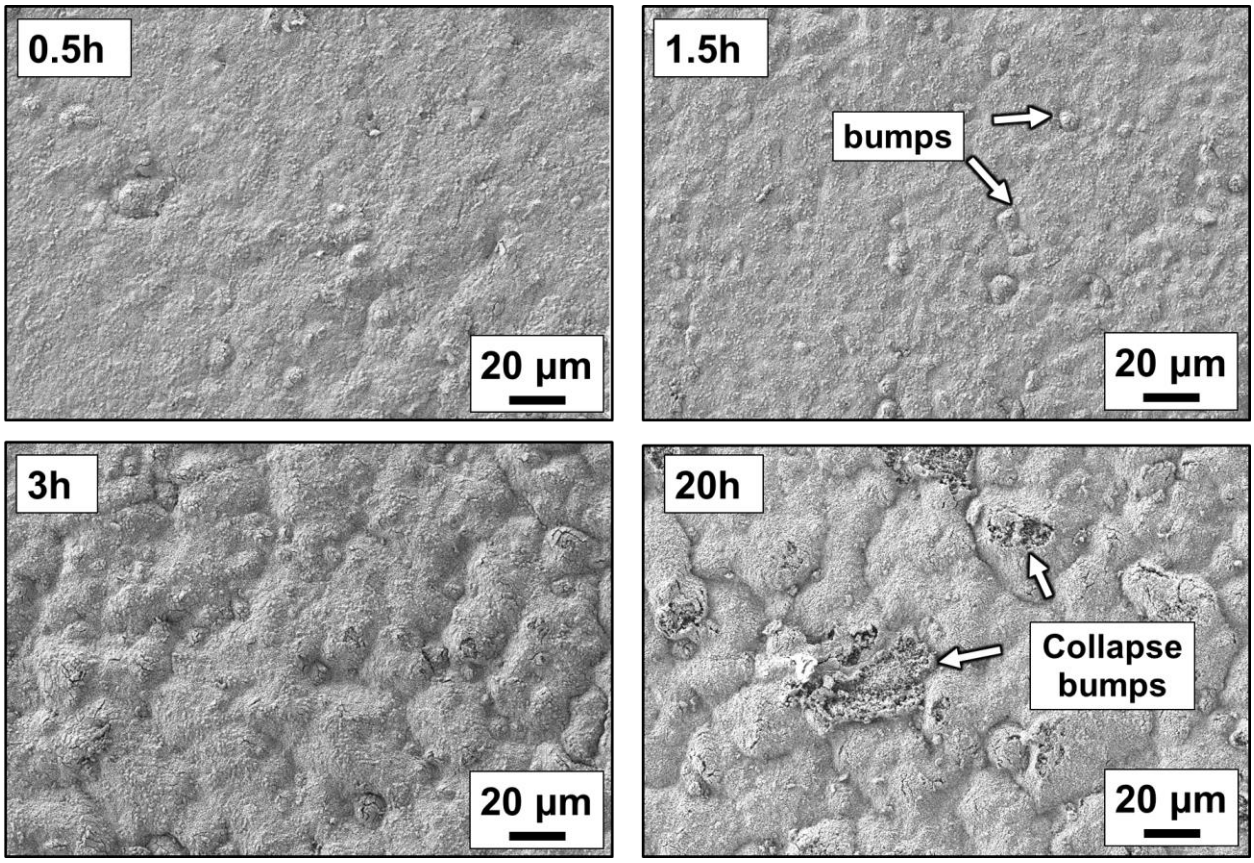

Fig. 11: Surface microstructural evolution at different oxidation stages of the 100h-annealed material with enhanced surface buckling effect.

4. Summary

In this work, the microstructural evolution during the phase decomposition of WCrY alloy at 1000 ℃ for up to 100 hours was studied. The mechanical properties and oxidation performance of the decomposed material were investigated and compared to its undecomposed counterpart. The key findings are as follows:

- The decomposition of WCrY at 1000 ℃ is a temporal process where the parent $(\alpha W, Cr)_0$ phase undergoes continuous separation into Cr-rich (αCr, W) and Cr-lean (αW, Cr) phases. (αCr, W) tends to form at grain boundaries and yttrium oxides. Over the course of decomposition, (αCr, W) starts as nanosized particles at 2 h and gradually coarsens to over 100 nm with occasional coalescence by 100 h. At 100 h, the Cr concentration in the (αCr, W) phases increases to near equilibrium. In contrast, the Cr concentration in the (αW, Cr) phases decreases to (17.8 ± 1.6) at.%, showing that equilibrium has not yet been reached.

- In terms of mechanical properties, a decrease in hardness due to compositional change but increase in strength due to additional phase boundaries after decomposition for 100 hours is observed. Flexural strength of the decomposed material maintains at ~1.1 GPa below 900℃, representing a 30 - 50% increase compared to the homogeneous microstructure. This enhancement is owing to the refined microstructure after decomposition and the phase boundary strengthening of (αCr, W). However, fracture toughness decreases by ~1 MPa·√m at elevated temperatures, compared to the homogeneous microstructure.
- The decomposed material in humid air for 20 hours exhibits two distinct stages of oxidation kinetics, contrasting with the single linear mass increase in the as-sintered material. During the first stage (0 - 3 h), characterized by inner oxide growth, there is a rapid linear increase followed by a gradual slowdown increase in mass change. The second stage (3 - 20 h), focusing on top chromia growth, shows a relatively "flat" mass change curve with subtle shifts, which is promising for long-term oxidation. Further investigation beyond 20 hours is necessary to fully evaluate the extended stability of the decomposed material in oxidizing environments. Additionally, the understanding of oxidation behaviour has primarily focused on the evolution of decomposed phases. The role of yttrium is not discussed, which needs further detailed investigation.

Acknowledgement

This work has been carried out within the framework of the EUROfusion Consortium, funded by the European Union via the Euratom Research and Training Programme (Grant Agreement No 101052200 - EUROfusion). Views and opinions expressed are however those of the author(s) only and do not necessarily reflect those of the European Union or the European Commission. Neither the European Union nor the European Commission can be held responsible for them. J.C. acknowledges the financial support by China Scholarship Council (CSC). The authors acknowledge Ralf Steinert from IMD-2, Forschungszentrum Jülich GmbH, Germany, for his assistance and instruction with FAST sintering process. CIME-UPM activities were supported by the Spanish "Agencia Estatal de Investigación" under the call “Proyectos de Generación de Conocimiento 2022” (3DPOSTHERMEC, PID2022-137274NB-C33PID). D.N.M., E.P., and T.W. also acknowledge funding by the EPSRC Energy Programme [grant number EP/W006839/1].

References

1. Litnovsky, A., et al., *Smart Tungsten-based Alloys for a First Wall of DEMO.* Fusion Engineering and Design, 2020. **159**: p. 111742.
2. Bolt, H., et al., *Plasma facing and high heat flux materials – needs for ITER and beyond.* Journal of Nuclear Materials, 2002. **307-311**: p. 43-52.
3. Klein, F., et al., *Oxidation resistance of bulk plasma-facing tungsten alloys.* Nuclear Materials and Energy, 2018. **15**: p. 226-231.
4. Maisonnier, D., et al., *A conceptual study of commercial fusion power plants. Final Report of the European Fusion Power Plant Conceptual Study (PPCS).* EFDA report number EFDA (05)-27/4.10, 2005. **1**.
5. Wegener, T., et al., *Development of yttrium-containing self-passivating tungsten alloys for future fusion power plants.* Nuclear Materials and Energy, 2016. **9**: p. 394-398.
6. Calvo, A., et al., *Self-passivating W-Cr-Y alloys: Characterization and testing.* Fusion Engineering and Design, 2017. **124**: p. 1118-1121.
7. Tan, X.Y., et al., *Evaluation of the high temperature oxidation of W-Cr-Zr self-passivating alloys.* Corrosion Science, 2019. **147**: p. 201-211.
8. Sal, E., et al., *Microstructure, oxidation behaviour and thermal shock resistance of self-passivating W-Cr-Y-Zr alloys.* Nuclear Materials and Energy, 2020. **24**: p. 100770.
9. Vilémová, M., et al., *Microstructure and phase stability of W-Cr alloy prepared by spark plasma sintering.* Fusion Engineering and Design, 2018. **127**: p. 173-178.
10. Wang, W.J., et al., *The influence of powder characteristics on densification behavior and microstructure evolution of W-Cr-Zr alloy consolidated by field-assisted sintering technology.* International Journal of Refractory Metals and Hard Materials, 2022. **108**: p. 105939.
11. Calvo, A., et al., *Manufacturing and testing of self-passivating tungsten alloys of different composition.* Nuclear Materials and Energy, 2016. **9**: p. 422-429.
12. Calvo, A., et al., *Manufacturing of self-passivating tungsten based alloys by different powder metallurgical routes.* Physica Scripta, 2016. **2016**(T167): p. 014041.
13. Litnovsky, A., et al., *New oxidation-resistant tungsten alloys for use in the nuclear fusion reactors.* Physica Scripta, 2017. **2017**(T170): p. 014012.

14. Wang, W.J., et al., *The influence of heating rate on W-Cr-Zr alloy densification process and microstructure evolution during spark plasma sintering.* Powder Technology, 2020. **370**: p. 9-18.
15. Wang, W.J., et al., *On grain growth and phase precipitation behaviors during W-Cr-Zr alloy densification using field-assisted sintering technology.* International Journal of Refractory Metals and Hard Materials, 2021. **98**: p. 105552.
16. Yang, S.P., et al., *Influence of the applied pressure on the microstructure evolution of W-Cr-Y-Zr alloys during the FAST process.* Fusion Engineering and Design, 2021. **169**: p. 112474.
17. Gottstein, G., *Physical foundations of materials science*. Vol. 3. 2004: Springer.
18. Terentyev, D., et al., *Development of irradiation tolerant tungsten alloys for high temperature nuclear applications.* Nuclear Fusion, 2022. **62**(8): p. 086035.
19. Andersson, J.O., et al., *Thermo-Calc & DICTRA, computational tools for materials science.* Calphad, 2002. **26**(2): p. 273-312.
20. Sobieraj, D., et al., *Composition Stability and Cr-Rich Phase Formation in W-Cr-Y and W-Cr-Ti Smart Alloys.* Metals, 2021. **11**(5): p. 743.
21. Porter, D.E., *The decomposition of tungsten-chromium solid solution.* Acta Metallurgica, 1967. **15**(5): p. 721-726.
22. Den Broeder, F.J.A. and W.G. Burgers, *An x-ray diffraction study of the decomposition of tungsten-chromium solid solution.* Acta Metallurgica, 1968. **16**(3): p. 265-268.
23. Naidu, S.V.N., A.M. Sriramamurthy, and P.R. Rao, *The Cr−W (Chromium−Tungsten) system.* Bulletin of Alloy Phase Diagrams, 1984. **5**(3): p. 289.
24. Hoffman, R.A., et al., *Study of phase transformations in chromium-tungsten films: microstructure and tribological properties.* Surface and Coatings Technology, 1994. **68-69**: p. 274-278.
25. Sal, E., et al., *High temperature microstructural stability of self-passivating W-Cr-Y alloys for blanket first wall application.* Fusion Engineering and Design, 2019. **146**: p. 1596-1599.
26. Veverka, J., et al., *Ultrafine-grained W-Cr composite prepared by controlled W-Cr solid solution decomposition.* Materials Letters, 2021. **304**: p. 130728.

27. Veverka, J., et al., *Decreasing the W-Cr solid solution decomposition rate: Theory, modelling and experimental verification.* Journal of Nuclear Materials, 2023. **576**: p. 154288.
28. Schneider, C.A., W.S. Rasband, and K.W. Eliceiri, *NIH Image to ImageJ: 25 years of image analysis.* Nature Methods, 2012. **9**(7): p. 671-675.
29. Guinea, G., et al., *Stress intensity factor, compliance and CMOD for a general three-point-bend beam.* International Journal of Fracture, 1998. **89**: p. 103-116.
30. Pastor, J., et al. *Nueva expresión del factor de intensidad de tensiones para la probeta de flexión en tres puntos*. in *Anales de Mecánica de la Fractura*. 1995. **12:** p.85-90.
31. Mishin, Y., *Solute drag and dynamic phase transformations in moving grain boundaries.* Acta Materialia, 2019. **179**: p. 383-395.
32. Hu, G.W., et al., *Combined effects of solute drag and Zener pinning on grain growth of a NiCoCr medium-entropy alloy.* Intermetallics, 2021. **136**: p. 107271.
33. Ramanarayan, H. and T.A. Abinandanan, *Grain boundary effects on spinodal decomposition: II. Discontinuous microstructures.* Acta Materialia, 2004. **52**(4): p. 921-930.
34. Deng, Y.-Y., et al., *Phase-field study of spinodal decomposition under effect of grain boundary**. Chinese Physics B, 2021. **30**(8): p. 088101.
35. Li, L., et al., *Segregation-driven grain boundary spinodal decomposition as a pathway for phase nucleation in a high-entropy alloy.* Acta Materialia, 2019. **178**: p. 1-9.
36. Rajeshwari K, S., et al., *Grain boundary diffusion and grain boundary structures of a Ni-Cr-Fe- alloy: Evidences for grain boundary phase transitions.* Acta Materialia, 2020. **195**: p. 501-518.
37. Zhou, X., et al., *Spinodal Decomposition in Nanocrystalline Alloys.* Acta Materialia, 2021. **215**: p. 117054.
38. Razumov, I.K., Y.N. Gornostyrev, and A.Y. Yermakov, *Kinetics of spinodal decomposition in driven nanocrystalline alloys.* Journal of Alloys and Compounds, 2007. **434-435**: p. 535-539.
39. Drescher, S., et al., *Softening by spinodal decomposition in Au–Cu–Ni–Pd–Pt high-entropy alloys.* Materials Science and Engineering: A, 2023. **887**: p. 145772.

40. Jeong, J.-I., et al., *Spinodal decomposition related to age-hardening and cuboidal structures in a dental low-carat gold alloy with relatively high Cu/Ag content ratio.* Gold Bulletin, 2014. **47**(1): p. 65-73.
41. Tejado Garrido, E.M., *Performance of structural materials for the DEMO divertor*. Doctoral dissertation, Universidad Politécnica de Madrid. Archivo Digital UPM, 2017. p. 214.
42. García-Rosales, C., et al., *Oxidation behaviour of bulk W-Cr-Ti alloys prepared by mechanical alloying and HIPing.* Fusion Engineering and Design, 2014. **89**(7-8): p. 1611-1616.
43. Hou, Q.-Q., et al., *Microstructure and its high temperature oxidation behavior of W-Cr alloys prepared by spark plasma sintering.* Materialia, 2019. **6**: p. 100332.
44. Hou, P., *1.10 Oxidation of Metals and Alloys*, in *Volume 1: Basic Concepts, High Temperature Corrosion, Shreir's Corrosion, Oxford*. 2010. p. 195-239.
45. Klein, F., et al., *Sublimation of advanced tungsten alloys under DEMO relevant accidental conditions.* Fusion Engineering and Design, 2019. **146**: p. 1198-1202.